Enhancement of surface activity in CO oxidation on Pt(110) through spatiotemporal laser actuation

L. Qiao, X. Li,[*] I. G. Kevrekidis,[†] and C. Punckt

Department of Chemical Engineering, Princeton University, Princeton, New Jersey 08544, USA

H. H. Rotermund

Department of Physics and Atmospheric Science, Dalhousie University, Halifax, Nova Scotia, Canada B3H 3J5

We explore the effect of spatiotemporally varying substrate temperature profiles on the dynamics and the resulting reaction rate enhancement of the catalytic oxidation of CO on Pt(110). The catalytic surface is "addressed" by a focused laser beam whose motion is computer controlled. The averaged reaction rate is observed to undergo a characteristic maximum as a function of the speed of this moving laser spot. Experiments as well as modeling are used to explore and rationalize the existence of such an optimal laser speed.

I. INTRODUCTION

A crucial component of chemical engineering process design is to locate optimal operating conditions, which yield optimized productivity, selectivity, and flexibility under safety and environmental constraints. Typically one searches for optimal *steady-state* conditions, possibly stabilized through feedback loops; yet it is also well known that non-steady-state operating conditions may lead to better average performance [1]. Examples of such chemical engineering processes include fast pressure swing adsorption [2] and reverse flow reactors [3]. Improvement of the average process performance under non-steady-state conditions (e.g., periodically varying reaction conditions) can sometimes be rationalized through certain resonances between the characteristic operation time scale (e.g., the period of the forcing) and the intrinsic time scales of the system [4].

Catalytic reaction systems often exhibit rich nonlinear dynamic behavior, including spatiotemporal patterns such as propagating reacting fronts, pulses, rotating spirals, and even chaos [5–7]. Since the emergence of these spatiotemporal patterns is governed by the system intrinsic time and length scales, catalytic systems may be promising testing fields for optimal non-steady-state operating policies [8]. The development of advanced surface resolving techniques such as photoemission electron microscopy [9,10], ellipsomicroscopy for surface imaging (EMSI) [11,12], and reflection anisotropy microscopy [13] has facilitated the observation of catalytic spatiotemporal patterns at the micron scale. Related advances in spatiotemporally addressing catalytic surfaces at the micron scale, in particular through computer-controlled laser beams, have enabled us to spatiotemporally modify local reaction conditions in real time: Pulses and fronts, the building blocks of spatiotemporal patterns, can be initiated, erased or guided through appropriate local laser actuation in

space and time [14,15]. Such light-induced control of spatiotemporal pattern formation can also be realized in other systems, e.g., the photosensitive Belousov-Zhabotinsky reaction [16].

In a previous experimental study of modifying the local catalytic surface activity in CO oxidation on Pt(110) through local laser actuation, it was discovered that optimal laser scanning policies exist, maximizing overall reaction (i.e., CO_2 production) rate when the system is close to the excitable regime [17]. The reaction conditions used in those experiments were selected in a way such that the system was initially at a CO-poisoned state (with Pt surface dominated by adsorbed CO which leads to low CO_2 production rate), but could become locally excited upon local laser heating. The actuation of the laser beam converts the local Pt surface to an excited state by increasing the local temperature and hence accelerating the desorption of CO. When the laser beam is kept at a fixed position, reacting oxygen pulses are periodically initiated around the laser heating spot, and propagate away causing a significantly higher local reaction rate. When the laser beam is scanned at a constant speed, it continuously locally excites the Pt surface [18]. Depending on the intensity of the laser, the spatiotemporal "policy" at which it scans the surface, its scanning speed, and the characteristic times required for the surface to return—after excitation—to the quenched state, different maxima in the overall CO_2 production rate were observed and partially rationalized in Ref. [17].

In order to systematically explore optimal operating conditions we choose a simple laser scanning policy (constant speed "dragging" along a one-dimensional path [18]) and attempt to establish a quantitative connection between the laser scanning policy and the corresponding overall CO_2 production rate. This is attempted through modeling of the appropriate catalytic reaction-diffusion system with spatiotemporal laser actuation. As a first step, we studied the simple case in which the laser spot scanned the surface in a fixed circular pattern at various speeds, through both numerical bifurcation analysis and simulations. By identifying a certain pulse instability associated with the dragging of the laser spot, our computational results could predict the existence of

─────────

[*]Present address: Merck Research Laboratories, West Point, PA 19486.

[†]Also at Program in Applied and Computational Mathematics (PACM), Princeton University, Princeton, NJ 08544.

a local maximum in overall CO_2 production rate while varying the laser scanning speed, in agreement with the experiments. The paper is organized as follows. We begin with a brief description of our model of CO oxidation on Pt(110) with local laser dragging. Computational results from numerical bifurcation analysis and transient simulations are then presented and discussed. We also briefly describe the experimental setup and present the experimental results; we conclude with a discussion of the relation between experiments and modeling, and possible extensions of the work.

II. MODELING

The experimental system of interest is the oxidation of CO on Pt(110); we therefore use the Krischer-Eiswirth-Ertl (KEE) reaction-diffusion model for this reaction [19]. The surface reaction follows a Langmuir-Hinshelwood mechanism:

$$CO + * \leftrightharpoons CO_{ads},$$

$$2* + O_2 \rightarrow 2O_{ads},$$

$$CO_{ads} + O_{ads} \rightarrow 2* + CO_2\uparrow,$$
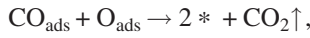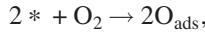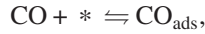
accompanied by a $1 \times 2 \rightarrow 1 \times 1$ phase transition of the Pt(110) surface due to CO adsorption. The equations for this kinetic model are

$$\dot{u} = k_u s_u p_{CO}\left[1 - \left(\frac{u}{u_s}\right)^3\right] - k_1 u - k_2 uv + \nabla \cdot (D_u \nabla u), \quad (1)$$

$$\dot{v} = k_v p_{O_2}[ws_{v_1} + (1-w)s_{v_2}]\left(1 - \frac{u}{u_s} - \frac{v}{v_s}\right)^2 - k_2 uv, \quad (2)$$

$$\dot{w} = k_3[f(u) - w], \quad (3)$$

where u, v, and w denote the surface coverage of CO, O, and the surface fraction of the 1×1 phase, respectively; s_u, s_{v1}, and s_{v2} are the sticking coefficients for CO adsorption, and for oxygen adsorption on the 1×1 phase and the 1×2 phase, respectively. k_u and k_v are the adsorption rate constants for CO and O_2, respectively. The rate constants k_1, k_2, and k_3 for the desorption, reaction, and surface phase transition are temperature dependent through the Arrhenius formula $k_i = k_i^0 \exp(-E_i/kT)$; T is the temperature of the single crystal. We used the parameters for Pt(110) given in Table II of Ref. [19] as follows:

$$u_s = 1, \quad v_s = 0.8, \quad s_u = 1, \quad s_{v_1} = 0.6, \quad s_{v_2} = 0.4,$$

$$k_u = 3.135 \times 10^5 \text{ s}^{-1} \text{ mbar}^{-1},$$

$$k_v = 5.858 \times 10^5 \text{ s}^{-1} \text{ mbar}^{-1},$$

$$k_i = k_i^0 \exp(-E_i/kT), \quad i = 1, 2, \text{ and } 3,$$

$$k_1^0 = 2 \times 10^{16} \text{ s}^{-1}, \quad E_1 = 38 \text{ kcal/mol},$$

$$k_2^0 = 3 \times 10^6 \text{ s}^{-1}, \quad E_2 = 10 \text{ kcal/mol},$$

$$k_3^0 = 10^2 \text{ s}^{-1}, \quad E_3 = 7 \text{ kcal/mol}.$$

We adopted the diffusion coefficients reported in Ref. [20],

$$D_u = \begin{bmatrix} D_{uf} & 0 \\ 0 & D_{us} \end{bmatrix},$$

where $D_{uf} = D_{uf}^0 \exp(-E_{uf}/kT)$, $D_{uf}^0 = 5 \times 10^{-3} \text{ cm}^2/\text{s}$, $E_{uf} = 10 \text{ kcal/mol}$ as in the $[1\bar{1}0]$ direction, and $D_{us} = D_{us}^0 \exp(-E_{us}/kT)$, $D_{us}^0 = 7 \times 10^{-4} \text{ cm}^2/\text{s}$, $E_{us} = 8.9$ kcal/mol as in the $[001]$ direction. The function $f(u)$ has been fitted to experimental data to give the rate of surface phase transition as a function of u, the coverage of CO, as follows:

$$f(u) = \begin{cases} 0 & \text{for } u \leq 0.2, \\ \dfrac{u^3 - 1.05u^2 + 0.3u - 0.026}{-0.0135} & \text{for } 0.2 < u < 0.5, \\ 1 & \text{for } u \geq 0.5. \end{cases}$$

In Eqs. (1)–(3) the temperature field is assumed to be homogeneous across the catalytic surface and prescribed by a single parameter T. When a laser beam is scanned across the sample surface, the local temperature of the catalytic surface around the laser spot is temporarily increased, leading to spatiotemporal heterogeneity in the surface temperature field. In order to model such a spatiotemporally heterogeneous temperature field, we make the following two simplifications [21,22]: (a) The heat generated by the CO oxidation reaction on the Pt(110) surface ($\sim 1 \text{ mW/cm}^2$) is neglected compared to the power of the laser beam [$\sim 1 \text{ W}$ for a crystal surface of 75 μm in diameter (size of the laser spot)]; (b) we consider that the local temperature profile inhomogeneity is established (and then vanishes) instantly as the laser beam is applied (and then removed). This is because the time scale associated with the local temperature change [$\sim 10^{-3} \text{ s}$, estimated from W^2/α, where W is the diameter of the laser spot (75 μm) and α is the thermal diffusivity of Pt ($\sim 10^{-1} \text{ cm}^2/\text{s}$)] is much smaller than the time scales of local adsorbate coverage change ($\sim 10^{-1} \text{ s}$ and $\sim 1 \text{ s}$), estimated from CO desorption with $1/k_1$ and CO diffusion with W^2/D_{uf}. Based on these two simplifications, the spatiotemporal change in the temperature field induced by a moving laser beam can be modeled as a temperature "bump" with fixed shape, cotraveling with the laser spot.

In the experiments, the laser spot is moved along a circular path on the sample surface at constant speed. Because the typical diameter of the circular path ($\sim 860 \mu$m) is significantly larger than the size of the laser spot ($\sim 75 \mu$m in diameter), it is informative to model the laser scanning in one dimension with periodic boundary conditions. A computational frame cotraveling with the laser spot is introduced. Based on the KEE model and the discussion above, we have the following equations for CO oxidation in a one-dimensional periodic domain with laser scanning in a co-moving frame:

$$u_t = k_u s_u p_{CO}\left[1 - \left(\frac{u}{u_s}\right)^3\right] - k_1 u - k_2 uv + (\bar{D}_u u_z)_z + c u_z,$$

$$(4)$$

$$v_t = k_v p_{O_2}[w s_{v_1} + (1-w)s_{v_2}]\left(1 - \frac{u}{u_s} - \frac{v}{v_s}\right)^2 - k_2 uv + c v_z,$$

$$(5)$$

$$w_t = k_3(f(u) - w) + c w_z, \qquad (6)$$

where c is the speed of the comoving frame (equal to the laser moving speed); z is the spatial coordinate in the comoving frame with $z \equiv x - ct$; $\bar{D}_u$ is the anisotropic diffusion coefficient approximated by a spatially periodic function, $\bar{D}_u \equiv (D_{uf} + D_{us})/2 + (D_{uf} - D_{us})/2 \sin(4\pi x/L)$; and the remaining symbols are the same as in Eqs. (1)–(3), except k_1, k_2, and k_3, which are now spatially dependent because of the nonuniform temperature field $T(z)$ due to local laser heating. In the computations, the local $T(z)$ heterogeneity due to the laser spot is approximated by a Gaussian profile.

III. COMPUTATIONAL RESULTS

For simplicity, we first consider the case where the diffusion of CO in our one-dimensional domain is *isotropic* (i.e., constant $\bar{D}_u$). With this assumption, the coverage profile of the adsorbate in a *static* observation frame eventually becomes periodic in both space and time, when a laser beam is periodically scanned across the domain at a fixed speed c. This oscillatory solution (in the static observing frame) corresponds to a *steady-state* solution in the comoving frame [i.e., of Eqs. (4)–(6)]. A Newton-Raphson iteration combined with pseudoarclength continuation is used for Eqs. (4)–(6) to compute and continue the corresponding steady coverage profiles as the laser dragging speed, c, is varied (that is also the speed of the resulting dragged pulse). The CO$_2$ production rate is then averaged over the entire domain for each steady coverage profile and plotted against c, as shown in Fig. 1. The reported enhancement is in comparison to the reaction rate at the quenched state (without laser illumination).

Note that the steady profiles of adsorbate coverage computed through pseudo-arclength continuation may be unstable (the dashed line in Fig. 1), which can lead to an estimate of the average CO$_2$ production rate very different from direct dynamic simulations (through time integration) at fixed c. This will be discussed in more detail at the end of this section.

In Fig. 1, when the laser dimensionless dragging speed is increased from zero to approximately 23 (at point 2, corresponding to approximately 129 μm/s), the steady profiles of the adsorbate coverage retain a pulselike appearance. Such pulselike profiles gradually start to "lag behind" the laser spot, as the laser dragging speed increases, which leads to a monotonic increase in the overall CO$_2$ production rate by 20% compared to the quenched state. Following the solution branch from point 2 to point 4 in Fig. 1, the pulselike struc-
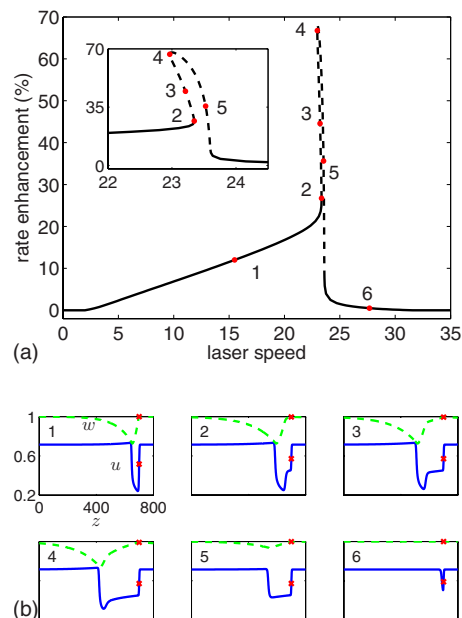

FIG. 1. (Color online) Enhancement in the CO$_2$ production rate as a function of the laser scanning speed for isotropic CO diffusion. The steady coverage profile is computed in a frame cotraveling with the laser spot. Stable (unstable) steady coverage profiles are marked in solid (dashed) lines. The inset shows a blow-up of the unstable branch. Representative coverage profiles are shown below, where the solid and dashed curves represent the coverage of CO and the fraction of the 1×1 phase, respectively. The coverage of CO and the fraction of the 1×1 phase at the center of the laser spot are marked by red crosses. Parameters used: Domain length $L = 800$, space discretization $\Delta x = 0.25$ with periodic boundary conditions. The local temperature field around the laser spot is approximated by a Gaussian profile ($\sigma = 2$), with a maximum temperature increase $\Delta T = 5$ K at the laser spot center $x = 700$. Reaction conditions: $T = 541$ K, $p_{CO} = 4.68 \times 10^{-5}$ mbar, $p_{O_2} = 1.33 \times 10^{-4}$ mbar. The unit dimensionless time and length correspond to real values of 1 s and ~ 5.6 μm, respectively. The unit dimensionless speed thus corresponds to a real speed of ~ 5.6 μm/s.

ture gradually dissolves and a "plateau" in the CO coverage profile starts to develop between the center of the laser spot and the lagging pulselike structure. The "pulse" now appears to consist of two distinct fronts—a leading and a trailing one. After point 4, the plateau also starts to shrink and finally disappears around $c = 24$. Such a process occurs in a very narrow range of c (approximately between 23 to 24) and causes a very sharp increase in the overall CO$_2$ production rate enhancement (up to 70%) followed by an immediate sharp decrease (down to approximately 5%), which is apparently associated with the development and disappearance of a wide plateau in the CO coverage profile. When the laser scanning speed is increased above 24, the rate enhancement quickly drops to zero.

The emergence of the pulselike structure and the plateau in CO coverage profile is thus seen to be intimately related to the rate enhancement. In order to better understand the nature of this relation, we explore the connection between the steady spatial coverage profiles and the dynamics of the KEE ordinary differential equation (ODE) model, as shown in Fig.
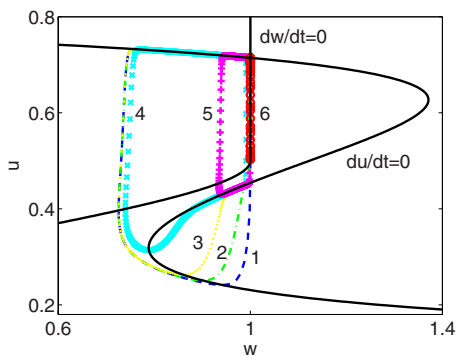
FIG. 2. (Color online) Phase portraits for steady coverage profiles at different c values (corresponding to points 1 through 6 in Fig. 1), see text.

2. It has been argued [23] that, since the oxygen adsorption is much faster than CO desorption, the temporal variation of oxygen coverage can be adiabatically eliminated for simplification, leading to a reduced two-variable model (for u and w). The corresponding nullclines of this two-dimensional model are plotted in Fig. 2 (solid lines). Representative dragged pulse coverage profiles in the comoving frame (e.g., points 1 through 6 in Fig. 1) correspond to limit cycles (periodic trajectories) of the ODE system (in z) obtained by setting the left-hand side of Eqs. (4)–(6) to zero. These u and w profiles are superposed on the simplified two-equation model nullclines in Fig. 2.

The trajectories corresponding to points 1 through 3 "reach down" to the lower branch of the $du/dt=0$ nullcline, confirming the pulselike nature of the pattern that results from laser dragging. The CO plateau structure, clearly seen in the spatial coverage profiles corresponding to points 3 through 5, is associated with the profile remaining close to the middle branch of the $du/dt=0$ nullcline. This "overlap" with the middle branch shrinks as the laser scanning speed c is increased. In dynamical systems terminology, this plateau structure is thus associated with a "canard" [24]. For point 6, the trajectory does not attain the middle branch of the $du/dt=0$ nullcline; it aligns with the $dw/dt=0$ nullcline.

Based on the discussion above, the relationship between the enhancement in CO_2 production rate and the laser dragging speed c, as shown in Fig. 1, can be partially rationalized as follows: When c is increased from zero up to values in the neighborhood of point 2 ($\sim$23.3), the laser spot locally excites the catalytic surface, creates and "drags along" a reacting pulse (e.g., point 1). Such a pulse remains attached to the laser spot; it starts becoming more spatially extended as c is increased, leading to a monotonic increase in production rate (appreciable adsorbed CO and oxygen coexisting over longer spatial extents). When c becomes too fast for the laser actuation to excite the local catalytic surface, the brief temperature increase effected by the passage of the laser spot only leads to a small local variation in the coverage profile (e.g., point 6). For values of c between the two limiting cases above (e.g., between points 2 and 5 in Fig. 1), the steady coverage profiles computed from pseudoarclength continuation become unstable. In this case, direct simulations must be used to find what the stable long-term behavior is, and thus estab-
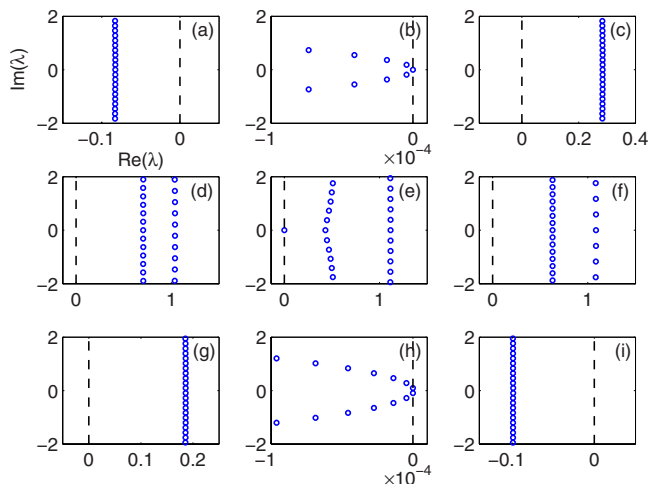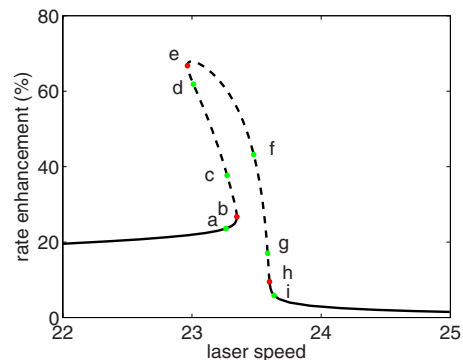

FIG. 3. (Color online) A blow-up picture of the unstable solution branch (dashed line) in Fig. 1. Points b, e, and h are significant bifurcation points. Following the solution branch from left to right, representative eigenvalue spectra (marked by circles) corresponding to the labeled points are plotted in the insets below. The position of zero is marked by a dashed line in the insets.

lish a connection between c and the corresponding rate enhancement (see below).

A blow-up of the unstable solution branch in Fig. 1 is shown in Fig. 3 along with the corresponding eigenvalue spectra of the system linearization in the neighborhood of the bifurcation points. These linearization spectra have been computed in a finite but long domain with periodic boundary conditions; computed eigenvalues are marked by circles, and the density of these circles is suggestive of continuous spectrum components for the infinite domain problem.

As we move from point a to point c, a "parabola" of eigenvalues crosses the imaginary axis from left to right. For our large but finite periodic problem, the leading eigenvalue [the eigenvalue(s) with largest real part on this parabola] is a single real one [as in inset (b)]. The initiation of the crossing of such an "eigenvalue parabola," corresponds to a saddle-node (SN) bifurcation followed by a large number of subsequent Hopf bifurcations. As c varies from point c to point d, the leading spectrum component appears to split in two. At point e a single real eigenvalue (whose path started close to the parabolic spectrum component farthest to the left from the imaginary axis) crosses the imaginary axis, corresponding to another SN bifurcation. From points f to g, the split
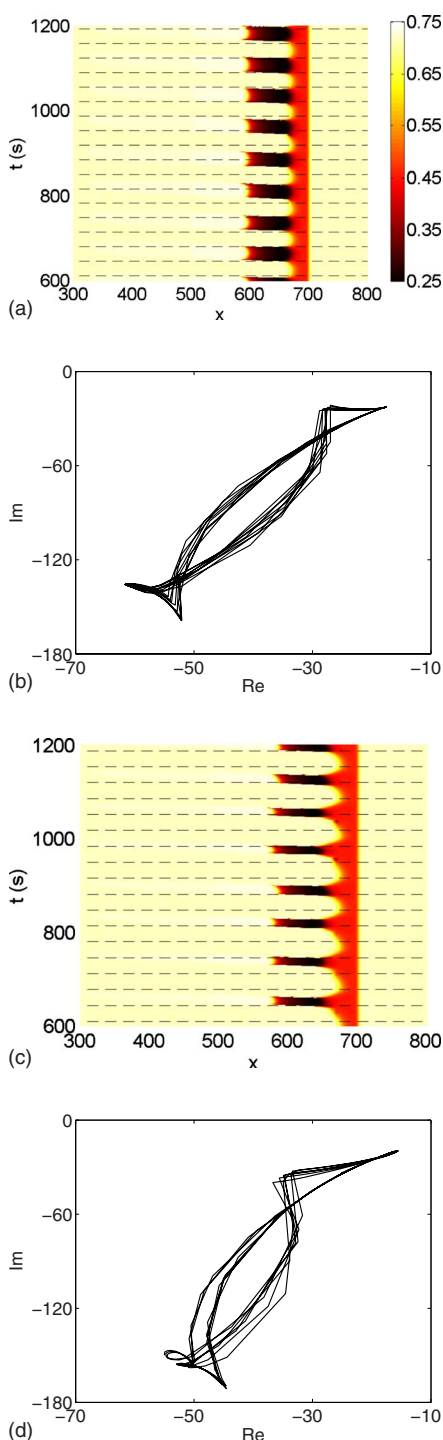
(a)

(b)

(c)

(d)

FIG. 4. (Color online) Space-time plots and phase portraits of CO coverage dynamics for different laser scanning speeds in the unstable regime. (a) and (c) Space-time plots of CO coverage (u) for $c=23.5$ and 23.6, respectively. (b) and (d) The corresponding phase portraits of the first fast Fourier transform component of the CO spatial coverage profile. When c is increased the system spends less time on average at a state with a long reacting tail; thus the overall CO_2 production rate is less in (c) as compared with (a). The time interval between dashed lines in (a) and (c) corresponds to L/c, that is, one "rotation" of the laser beam along the periodic domain.

spectrum components appear to merge again into a single component, which then crosses the imaginary axis from right to left (see point h). The leading eigenvalues of this new parabolic spectrum component (the last ones to cross to stability) are now a conjugate pair (in contrast to point e). The crossing of such a component of the spectrum appears in our finite domain case (from point g to point i) as a chain of Hopf bifurcations. Continuous eigenvalue spectrum crossing has been shown to be associated with the emergence of "chemical turbulence" for CO oxidation in an excitable medium [25].

For values of c for which the dragged pulse solutions are unstable, direct simulation is used to establish the nature of the observed dynamics (and to find the corresponding average reaction rate). Phase diagrams of the long-term dynamics for such simulations appear quasiperiodic or mildly chaotic, and do not repeat exactly (as shown in Fig. 4). For sufficiently large domains (as was the case here), the approximate period of the oscillations is not affected by the domain length. In this regime, as c is increased, the system spends less time on average in states with a long, reacting pulselike tail, which leads to a decrease in the overall (space-time averaged) CO_2 production rate. This is consistent with the (spatiotemporally) averaged reaction rate monotonically decreasing as c varies from points e through h in Fig. 3.

Anisotropic CO diffusion. To incorporate the effect of diffusion anisotropy for the adsorbed CO on Pt(110), we approximate the anisotropic diffusion coefficient with a spatially periodic function, $\bar{D}_u \equiv (D_{uf}+D_{us})/2+(D_{uf}-D_{us})/2 \sin(4\pi x/L)$, where D_{uf} and D_{us} correspond to the coefficients of CO diffusion on Pt(110) in the fast ($[1\bar{1}0]$) and in the slow ($[001]$) directions, respectively. The interaction between laser scanning and strong anisotropic CO diffusion is illustrated in Fig. 5, which shows that the reacting tails only exist in regions where the local CO diffusion is slow. To visually enhance this phenomenon, and also to show how different the instantaneous pulse profiles can be as the laser rotates on the surface, Fig. 5 employs diffusion coefficient values 6 times as large as the ones reported in [20] (but with the correct anisotropy ratio). Resetting D_{uf} and D_{us} to their experimentally reported values [20], time integrations of Eqs. (4)–(6) show periodic or apparently quasiperiodic transient behavior (Fig. 7). In both cases we average the reaction rate over both the domain length and a long enough time interval to compute the corresponding average enhancement in CO_2 production rate shown in Fig. 6.

When c is varied between 0 and approximately 23, the dynamics in the comoving frame converge to a stable oscillatory state with a period of $L/(2c)$. During the oscillations, the length of the reacting tail only slightly varies as the local CO diffusion coefficient modulates (not shown). Similar behavior has been observed for larger c (i.e., >24), where the width of local coverage profile around the laser spot slightly modulates. Compared with the isotropic case, the averaged rate enhancement shows the same qualitative behavior for the two limiting cases: For smaller c the rate enhancement gradually increases as c is increased; for large c the rate enhancement suddenly decreases as c is increased. When c is in the intermediate range 23–24 (associated with instability
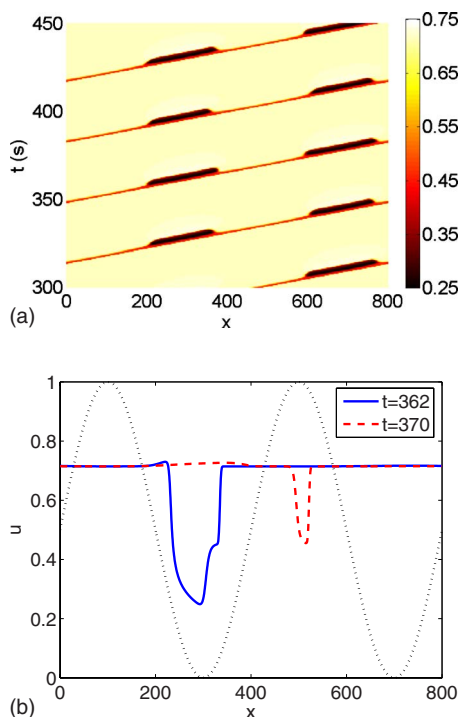
(a)

(b)

FIG. 5. (Color online) Laser scanning in the presence of strong anisotropic CO diffusion. (a) Space-time plot of CO coverage in a frame cotraveling with the laser spot; (b) representative instantaneous snapshots of the CO coverage profile. The anisotropic diffusion of CO is approximated by a periodic diffusion coefficient with a period of $L/2$ [dotted line in (b)], $\bar{D}_u \equiv (D_{uf}+D_{us})/2+(D_{uf}-D_{us})/2 \sin(4\pi x/L)$, where D_{uf} and D_{us} correspond to the diffusion coefficient values along the fast and slow directions on Pt(110), respectively, $D_{uf}/D_{us}=3$, $c=23.3$.

in the isotropic case), the system can show distinct quasiperiodic transient behavior: For c close to the lower boundary of this interval the system exhibits oscillations similar to those of the isotropic case [Fig. 7(b)]; for c close to the upper boundary, more complex oscillations can be observed, as
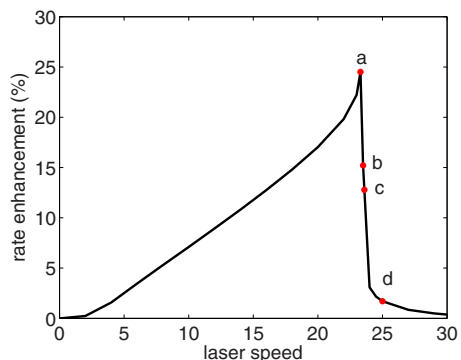

FIG. 6. (Color online) Averaged rate enhancement in CO_2 production as a function of laser scanning speed for anisotropic CO diffusion. For a fixed laser scanning speed, the CO_2 production rate is computed based on the spatiotemporal coverage profile, averaged over the entire domain and a sufficiently long time interval. D_{uf} and D_{us} are estimated from experimental data [20]; $D_{uf}/D_{us}=3$.
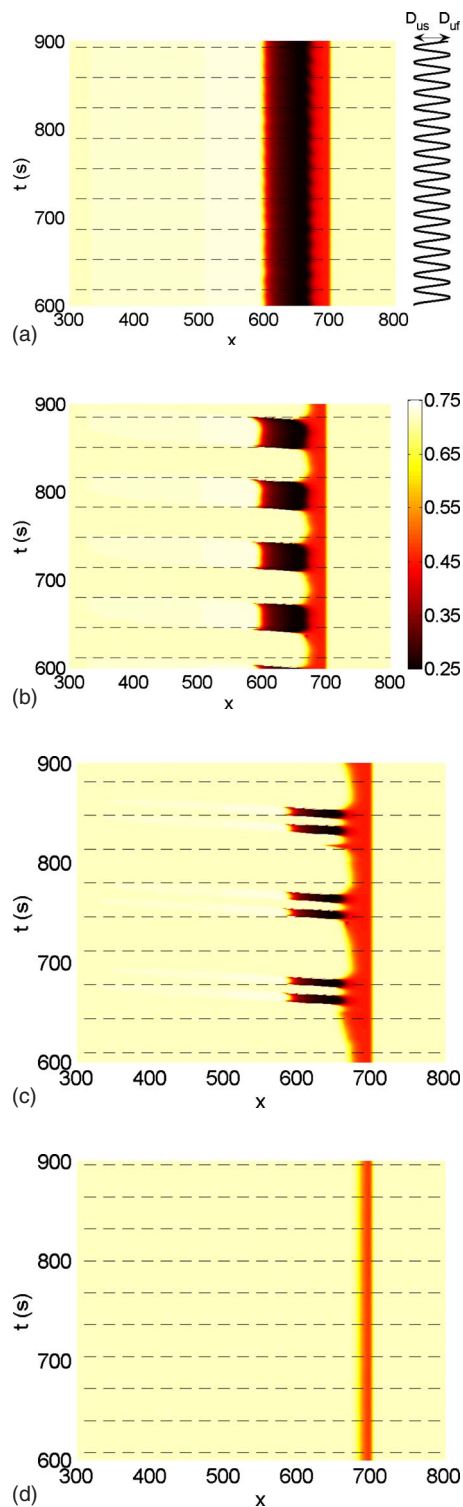

(a)

(b)

(c)

(d)

FIG. 7. (Color online) Phase portraits for anisotropic CO diffusion at different laser scanning speeds. The local CO diffusion coefficient at $x=700$ is plotted on the right-hand side of plot (a). (a) $c=23.3$, (b) $c=23.5$, (c) $c=23.6$, (d) $c=25$.

shown in Fig. 7(c). By comparing the position of reacting tails in Fig. 7(c) with the corresponding spatial profile of $\bar{D}_u$, we find that the reacting tails occur only along the slow diffusion directions (when the local $\bar{D}_u$ is small). This sug-

gests that the local periodic change in CO diffusion coefficient as the laser spot moves along a ring can have a strong impact on the local dynamics; it can, for example, temporarily eliminate a reacting tail and then reestablish it [see the small time gap in Fig. 7(c) when the reacting tail disappears]. As in the isotropic case, the averaged rate enhancement in this range of c monotonically decreases as c is increased.

IV. EXPERIMENTS

The simplest motion of a temperature heterogeneity on the platinum surface would be a linear one, on an infinitely extended catalyst. This cannot be realized in the experiment. The easiest consistent approach is to use a protocol where the laser spot moves on a circle with large circumference. This is experimentally feasible and makes a comparison with theory possible. Circular movement was tentatively explored in a previous study [17]; however, the resulting surface dynamics and changes in reaction rate were not analyzed in detail. Here, we show experimental results, focusing on reaction enhancement and the influence of the laser spot on the reaction patterns; we also compare to the theoretical results presented in the first part of the paper.

Experiments are performed using a Pt(110) single crystal with 10 mm diameter located in an ultrahigh vacuum chamber. For accurate control of the reaction parameters (temperature, CO and oxygen partial pressures), the chamber is equipped with a computer-controlled gas dosing system, that allows for adjusting the partial pressures of carbon monoxide and oxygen. The platinum sample is heated from the back with a halogen lamp. For sample preparation and characterization, the chamber is equipped with Ar-ion sputtering and low-energy electron diffraction. A tube (~38 mm in diameter) with a conelike ending (~4 mm in diameter) is placed about 2 mm away from the sample surface. It connects the reaction chamber with a differentially pumped quadrupole mass spectrometer (QMS) used for analysis of the reaction products. This way, a large fraction of the carbon dioxide produced during the reaction can be detected, providing an estimate of the overall surface reaction rate. The carbon monoxide signal detected by the QMS was stored on a computer.

Concentration patterns of CO and oxygen on the sample surface are imaged at a rate of 25 images per second using ellipsomicroscopy for surface imaging [11,12]. They are recorded with a video CCD camera. The background of the video signal is subtracted and the signal is contrast enhanced in real time using a downstream Argus 20 image processing unit from Hamamatsu and stored on a video recorder. The surface reaction can be locally manipulated by an argon ion laser beam which is focused onto the platinum crystal. The spot size of the laser is approximately 75 μm in diameter. Two computer-controlled mirrors allow for controlled motion of the laser spot on the sample surface. Special motion protocols (such as linear or circular trajectories of the laser spot) can be programmed using LabView. The partial pressures of oxygen and CO are also controlled through this software. The experimental setup is sketched in Fig. 8.

At the beginning of each experiment, the laser beam is focused to a fixed position on the sample surface for several
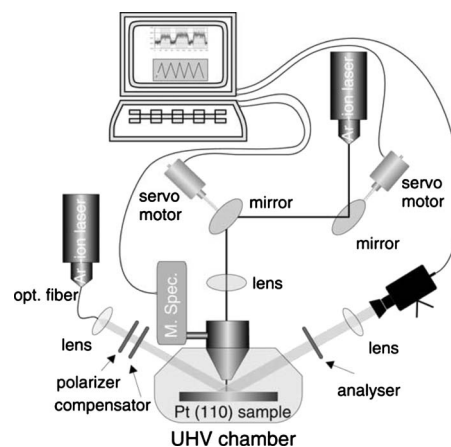

FIG. 8. Schematic view of the experimental setup, not to scale. See the text for details. Reproduced from [17].

minutes, until the temperature of the crystal equilibrates. This is necessary because the laser spot not only produces a strongly located temperature increase but additionally slightly increases the mean crystal temperature (by a few K). The laser beam is then scanned across the sample surface with a constant speed for 40 s, following a fixed circular path with a circumference of approximately 2.7 mm. This is illustrated in Fig. 9. The scanning of the laser beam is stopped for 1 minute every time before a different scanning speed for the laser beam is applied; at each speed several measurements are performed and their results in terms of reaction rate increase are averaged.

In EMSI images, dark surface area is associated with more reactive, predominantly oxygen covered surface. When the laser spot moves, a dark tail can be observed: The laser spot removes some adsorbed CO in its path. Since CO poi-
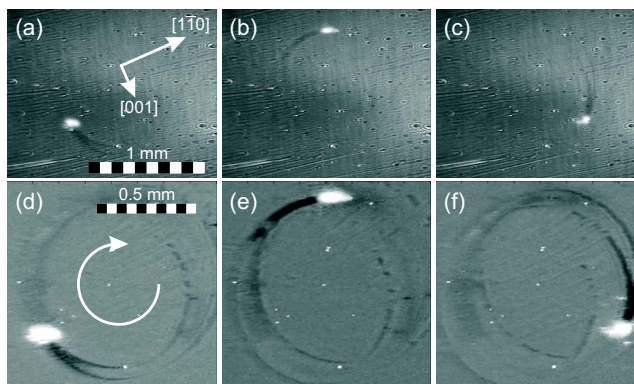

FIG. 9. (Color online) Circular motion of the laser spot across the platinum catalyst. (a)–(c) raw data, (d)–(f) images after additional background subtraction, contrast enhancement, and cropping. The time difference between the snapshots is 0.96 s. The crystal orientation is indicated in (a). Diffusion along the [1$\bar{1}$0] axis is faster (by an estimated factor of 2–3) than in the [001] direction. The laser spot is visible as a bright white area in the images. Due to the laser motion, a "tail" develops behind the spot. The reaction parameters are $P_{Laser}=640$ mW, $p_{O_2}=3.00\times10^{-4}$ mbar, $p_{CO}=8.43\times10^{-5}$ mbar, and $T=513$ K.
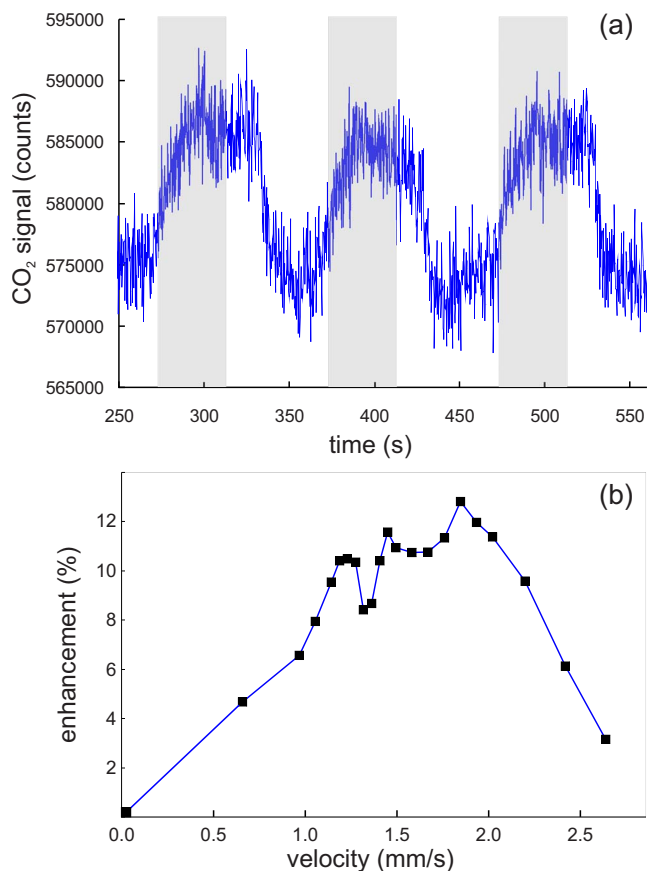
FIG. 10. (Color online) Enhancement of CO_2 production. (a) QMS signal; the laser spot is only moving during the shaded time intervals with a velocity of 0.91 mm/s. (b) Average enhancement for different velocities of the laser spot. The reaction parameters are $P_{Laser}=640$ mW, $p_{O_2}=3.00\times10^{-4}$ mbar, $p_{CO}=8.60\times10^{-5}$ mbar, and $T=512.5$ K.

sons the catalytic surface, its removal increases the catalytic activity. In addition to the one-dimensional theoretical observations in the first part of this paper, we see here the full two-dimensional structure of the laser-induced reactive surface area. At a certain distance from the laser spot, the tail divides, and a "swallowtail" composed of two narrow "tongues" can be seen. Figure 10(a) shows the CO_2 signal measured by the QMS. During the periods of laser spot motion (shaded regions) the CO_2 signal is increased. The delay between stopping the laser spot motion and associated decrease of the CO_2 production rate is due to the slow time scale of the differential pumping of the QMS.

We measure the increase of the carbon dioxide signal as a function of the laser spot velocity. The results are shown in Fig. 10(b). We observe that the average reaction rate increases for velocity values up to about 1.8 mm/s. For higher velocities, the enhancement falls precipitously until the laser spot moves so fast that no enhancement can be measured. When all other reaction parameters are kept fixed, there exists a certain velocity of the laser spot at which the enhancement is at it's maximum. We call this velocity value the "optimal velocity." The experimental curve agrees qualitatively with theory: A slow increase of the reaction rate is
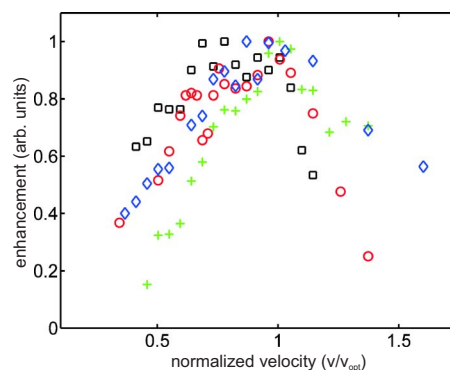

FIG. 11. (Color online) Reaction rate enhancement at different experimental conditions: Each enhancement curve is normalized with respect to its optimum velocity and maximum enhancement of the CO_2 formation. The reaction conditions were $P_{Laser}=640$ mW, $p_{O_2}=3.00\times10^{-4}$ mbar, $p_{CO}=8.60\times10^{-5}$ mbar, and $T=512.5$ K for experiments *A* (black squares) and *B* (red circles), and $p_{CO}=8.43\times10^{-5}$ mbar, and $T=513$ K for experiments *C* (green crosses), and *D* (blue diamonds).

followed by a fast decrease after the optimal velocity has been exceeded. This has been observed in our computations both for isotropic and for anisotropic diffusion coefficients; in the case of anisotropic diffusion the dragged pulse profile varies along the laser path because the diffusion coefficient also varies. The variation in the length of the pulse tail in the three snapshots of Fig. 9 is the result of the varying orientation of laser motion with respect to the crystal axes (and the associated CO diffusion coefficient variation).

Figure 11 shows the results of experiments at different reaction conditions, normalized with respect to the optimal velocity of each experiment. The qualitative behavior of the reaction enhancement appears similar in all cases shown. The experimental curves exhibit a clear maximum in the overall rate enhancement as the laser scanning speed is varied, in qualitative agreement with the computational results shown above. It is interesting to observe certain secondary reaction extrema "on the way" to the overall maximum as the laser spot velocity increases, e.g., at $v=1.35$ mm/s, Fig. 10(b). These were not observed in our one-dimensional modeling, and they most probably should be attributed to the two-dimensional nature of the experimental patterns.

As the laser moves on the catalytic surface, it locally shifts the system into an excitable state. This results in the development of a reactive "tail" behind the laser spot. The length and the width of this tail varies with the spot velocity as clearly seen in Fig. 12. Qualitatively, the variation of the average tail length with the laser dragging speed mimics the variation of the reaction rate enhancement both in modeling and in experiments: The tail initially becomes longer and then precipitously disappears as the speed is increased. However, due to the development of two "tongues" in the back of the tail, a clear definition of the tail length in the experiment is somewhat difficult. We (rather arbitrarily) choose the distance between the laser spot and the point where the tail visibly splits as a measure of the tail length. With increasing laser speed the tail becomes longer and narrower. In Fig. 12(d) the length of the tail has increased further, yet the
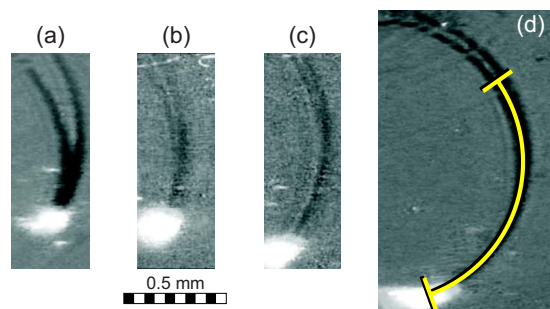
FIG. 12. (Color online) Length of the dark reactive tail at different velocities. (a) $v=0.94$ mm/s, $l=0.23$ mm, (b) $v=1.2$ mm/s, $l=0.38$ mm, (c) $v=1.8$ mm/s, $l=0.53$ mm, (d) $v=2.6$ mm/s, $l=0.79$ mm, parameters as in Fig. 9. The tail length is measured from the center of the laser spot to the point where the reactive tail splits, as indicated in (d).

reaction enhancement is almost negligible. This appears counterintuitive, since in the theoretical part of this paper we saw a clear correlation between tail length and reaction rate enhancement. However, the one-dimensional modeling ignores the width (and overall two-dimensional structure) of the tail; this makes direct comparison between the two-dimensional experiment and the one-dimensional theory difficult. We expect to report on a more quantitative comparison, based on full two-dimensional simulations, in a future presentation. For very high laser speeds in the experiment—as well as in the one-dimensional model—the reactive tail completely vanishes, since the thermal energy deposited per time and surface area in the catalytic surface no longer provides a sufficient local temperature increase to excite the system.

V. SUMMARY AND CONCLUSIONS

Following our initial experimental study [17] on improving catalytic surface activity through time-dependent operating policies, we performed here a systematic exploration of the effect of laser spot motion on the average reaction rate of CO oxidation on a Pt(110) surface. Quantitative relations between overall rate enhancement and the laser scanning speed, for both isotropic and anisotropic CO diffusion, have been obtained through numerical bifurcation analysis and direct simulations. A characteristic local maximum in the rate enhancement (gradual increase followed by precipitous drop) has been observed in both cases. The local maximum for isotropic CO diffusion was associated with the development of a pulse instability caused by laser dragging and apparently involving the dragged pulse continuous spectrum. When anisotropic CO diffusion is included in the model, and for a wide range of laser scanning speeds, the system exhibits comparable averaged rate enhancement response; yet the anisotropy has a significant qualitative effect on the detailed dynamics (including quasiperiodicity and even mild spatiotemporal chaos). The computational results are supported by experimental observations showing a qualitatively comparable increase of averaged reaction rate with laser scanning velocity. Optimal velocities were obtained experimentally for a range of different reaction conditions. Experimental observations revealed an interesting two-dimensional structure of the dragged pulse "reactive tail;" this clearly suggests that full two-dimensional modeling, taking into account diffusion transverse to the pulse motion, is required for a more quantitative comparison of theory with experiments. We are currently working toward such a fully two-dimensional model study. The laser motion explored in this paper was, in some sense, the simplest spatiotemporal one: Effectively one-dimensional with constant speed. Spatiotemporally more complex motions, such as those presented in [17], possibly also containing a stochastic component [26], should provide a rich field of study.

[1] J. E. Bailey, Chem. Eng. Commun. **1**, 111 (1974).

[2] D. M. Ruthven, S. Farooq, and K. S. Knaebel, *Pressure Swing Adsorption* (Wiley, New York, 1993).

[3] Y. S. Matros and G. A. Bunimovich, Catal. Rev.-Sci. Eng. **38**, 1 (1996).

[4] I. G. Kevrekidis, L. D. Schmidt, and R. Aris, Chem. Eng. Sci. **41**, 1263 (1986).

[5] M. C. Cross and P. C. Hohenberg, Rev. Mod. Phys. **65**, 851 (1993).

[6] R. Imbihl, Catal. Today **105**, 206 (2005).

[7] R. Imbihl and G. Ertl, Chem. Rev. **95**, 697 (1995).

[8] E. Machado, G. M. Buendia, P. A. Rikvold, and R. M. Ziff, Phys. Rev. E **71**, 016120 (2005).

[9] H. H. Rotermund, W. Engel, M. Kordesch, and G. Ertl, Nature (London) **343**, 355 (1990).

[10] W. Engel, M. E. Kordesch, H. H. Rotermund, S. Kubala, and A. von Oertzen, Ultramicroscopy **36**, 148 (1991).

[11] H. H. Rotermund, G. Haas, R. U. Franz, R. M. Tromp, and G. Ertl, Science **270**, 608 (1995).

[12] H. H. Rotermund, Surf. Sci. **386**, 10 (1997).

[13] C. Punckt, F. S. Merkt, and H. H. Rotermund, New J. Phys. **9**, 213 (2007).

[14] J. Wolff, A. G. Papathanasiou, I. G. Kevrekidis, H. H. Rotermund, and G. Ertl, Science **294**, 134 (2001).

[15] L. Qiao, I. G. Kevrekidis, C. Punckt, and H. H. Rotermund, Phys. Rev. E **73**, 036219 (2006).

[16] R. Tóth, V. Gáspár, A. Belmonte, M. C. O'Connell, A. Taylor, and S. K. Scott, Phys. Chem. Chem. Phys. **2**, 413 (2000).

[17] A. G. Papathanasiou, J. Wolff, I. G. Kevrekidis, H. H. Rotermund, and G. Ertl, Chem. Phys. Lett. **358**, 407 (2002).

[18] J. Wolff, A. G. Papathanasiou, H. H. Rotermund, G. Ertl, X. Li, and I. G. Kevrekidis, Phys. Rev. Lett. **90**, 018302 (2003).

[19] K. Krischer, M. Eiswirth, and G. Ertl, J. Chem. Phys. **96**, 9161 (1992).

[20] A. von Oertzen, H. H. Rotermund, and S. Nettesheim, Surf. Sci. **311**, 322 (1994).

[21] J. Cisternas, P. Holmes, I. G. Kevrekidis, and X. Li, J. Chem. Phys. **118**, 3312 (2003).

[22] J. Cisternas, P. Holmes, and I. G. Kevrekidis, Physica D **177**, 71 (2003).

[23] M. Bär, N. Gottschalk, M. Eiswirth, and G. Ertl, J. Chem. Phys. **100**, 1202 (1994).

[24] J. Moehlis, J. Nonlinear Sci. **12**, 319 (2002).

[25] M. G. Zimmermann, S. O. Firle, M. A. Natiello, M. Hildebrand, M. Eiswirth, M. Bär, A. K. Bangia, and I. G. Kevrekidis, Physica D **110**, 92 (1997).

[26] J. Wolff, A. G. Papathanasiou, H. H. Rotermund, G. Ertl, M. A. Katsoulakis, X. Li, and I. G. Kevrekidis, Phys. Rev. Lett. **90**, 148301 (2003).